# D3.2 Effects of Thermal Cycling on Sealants of Different Compositions under Confinement for CCS Applications

CEMENTEGRITY Deliverable 3.2, v. 1
Published 2025-01-31

Authors: Li, K., Pluymakers, A.
Rock Mechanics Lab, Delft University of Technology, the Netherlands

Reviewed by: Reinier van Noort (IFE Technology, Norway)

**Keywords**: *CCS, Well integrity, Sealants, Thermal cycling, Confinement, Thermal stress, Tensile strength*

## Summary:

In carbon capture and storage (CCS) wells, the sealing integrity of sealants under thermal cycling is crucial for ensuring permanent CO2 storage. Li and Pluymakers (2014) previously investigated the impact of cyclic thermal shocks on four sealants of different compositions, employing quenching and flow-through methods without confinement. The tested sealants included two ordinary Portland cement (OPC)-based blends (S1 and S2), a novel OPC-based blend with CO2-sequestering additives (S3), and a calcium aluminate cement (CAC)-based blend tailored for CCS applications (S4). They observed crack formation in S1, S2, and S4 samples, while S3 samples maintained integrity throughout both types of unconfined thermal-shocking experiments, suggesting thermal diffusivity as a critical determinant of sealant ability to withstand thermal shocks. In this study, we extend the investigation by examining the efficacy of these sealants under strong thermal cycling with confinement. Using a triaxial deformation setup, sealant samples are subjected to 1.5 or 10 MPa confinement and subjected to eight cycles of 20 °C water flow-through after heating to 120 °C. We utilize microscopic X-ray tomography (32 µm/voxel), helium pycnometry, and unconfined compressive tests to assess sealant performance before and after thermal treatment. Results indicate that all sealant samples maintain integrity without cracking under confinement, with increases in strength accompanied by decreased porosity. Experiments conducted under 10 MPa confinement even exhibit more enhanced strength and reduced porosity than those at 1.5 MPa. Furthermore, we calculate the thermal stress induced in unconfined flow-through experiments by Li and Pluymakers (2014). We find that thermal stress induced in each of their unconfined experiment exceeds the tensile strength of the respective sealant, except for S3. This fact, together with comparably low thermal diffusivity, leads to crack formation in S1, S2, and S4 samples after the thermal treatment. In this study with confined experiments, thermal stress is still greater than tensile strength for all sealants except S3. However, the confinement not only suppresses the crack formation by increasing the stiffness of the sealant during thermal cycling but also strengthens the sealant with a reduction in porosity. This

study together with Li and Pluymakers (2014) points out properties of a sealant that determine its efficacy to tolerate thermal cycling and provides novel experimental approaches to test the interplay of these properties. In light of our findings, we conclude that sealants with high tensile strength, high thermal diffusivity, low Young's modulus, and low thermal expansion coefficient are optimal candidates for withstanding cyclic thermal stress in CCS wells.

***Publication status:***
*This manuscript is under review at Cement and Concrete Research*

Note: this is an additional deliverable compared to the list published in the project proposal, given the expanded scope of the experimental program of WP3.

## 1 Introduction

Carbon capture and storage (CCS) technology has gained significant attention as a promising approach to mitigating global climate change by capturing $CO_2$ emissions and storing them in subsurface formations like depleted oil and gas reservoirs or saline aquifers (Metz et al., 2005; Haszeldine, 2009; Selma et al., 2014; Budinis et al., 2018; Bui et al., 2018). Successful implementation of CCS relies on the permanent containment of $CO_2$ within targeted reservoirs. However, the periodic injection of pressurized cold $CO_2$ into warm reservoirs during CCS operations induces cyclic temperature fluctuations, the precise intensity, rate, and frequency of which remain uncertain (Alnes et al., 2011; Eiken et al., 2011; Yoo et al., 2013; Samara et al., 2022).

In scenarios where $CO_2$ injection occurs into offshore reservoirs (c.f. the planned Portos project in the Netherlands, and Northern Lights project in Norway) at depths of 2 to 3 km, reservoir temperatures typically range from 80 to 120°C, while the injected $CO_2$ may have temperature as low as 0 °C. This can lead to temperature fluctuations of up to 100 °C during periodic injection, resulting in cyclic shrinkage and subsequent expansion in the wellbore and subsurface formations (Eiken et al., 2011; Lescanne et al., 2011; Yoo et al., 2013). Consequently, micro-annuli between wellbore casing, cement sheath, and wall-rock, as well as cracks in the cement, may be induced, posing a significant challenge to the safe and sustainable geological storage of $CO_2$ (Carpenter et al., 1992; Carey et al., 2007; Roy et al., 2016; Vilarrasa and Rutqvist, 2017).

Ordinary Portland cement (OPC) is commonly used as the main sealant in depleted oil and gas wells targeted for CCS due to its reliable performance and cost-effectiveness (Parker et al., 2009; Santra and Sweatman, 2011; Lesti et al., 2013). However, the sealing integrity of OPC-based wellbores may be vulnerable to deterioration under strong temperature fluctuations during cyclic $CO_2$ injection and storage. While some studies have investigated the effects of thermal cycling on the integrity of wellbore samples consisting of OPC, the focus has primarily been on sealing ability at interfaces between casing, cement, and rock, leaving the integrity of the cement material itself during thermal shocks largely unexplored (Albawi et al., 2014; Lund et al., 2015; De Andrade et al., 2015).

Moreover, the efficacy of alternative sealants, such as calcium aluminate cement (CAC), remains uncertain under temperature fluctuations. CAC offers advantages over OPC, such as higher early strength gain and enhanced acid resistance, making it attractive for CCS applications. However, its behavior under thermal cycling requires further investigation (Barborak, 2010; Dugonjic-Bilic et al., 2011).

To address these gaps, Li and Pluymakers (2024) previously investigated the sealing integrity of four sealant compositions under thermal shocks relevant to carbon capture and storage (CCS) applications. Alongside two different ordinary Portland cement (OPC)-based reference sealants (S1 and S2), they tested two novel blends designed for future CCS wells (S3 and S4). S3 is also OPC-based but contains crushed peridotite primarily composed of olivine (Kvassnes and Clausen, 2020; Kvassnes and Clausen, 2021), and S4 is CAC-based. In their study, they applied the thermal shock without confinement by either quenching 120 °C sealant samples into 6 L water bath at 20 °C, or flowing 20 °C water through 120 °C samples at 80 mL/min for 2 min. The shock was repeated eight times in both methods. They found that, only S3 maintained integrity, while all other sealants lost integrity by crack formation after both thermal-shocking experiments, suggesting the potential of S3 as an optimal sealant for CCS applications. Remarkably, they attributed the success of S3 to withstand thermal shocks to its comparably high thermal diffusivity compared to other sealants. However, both types of thermal-shocking experiments by Li and Pluymakers (2024) were conducted without confinement. In actual $CO_2$ storage environments, such as depths of 1 km (Kirby et al., 2001; Alnes et al., 2011; Zhang et al., 2022), the wellbore including sealant sheath would experience confining pressures of up to 10 MPa.

In this study, to understand how sealants behave under confinement, we further investigate the effects of thermal cycling on the aforementioned four sealants at a confining pressure of 1.5 or 10 MPa. We adopt flow-through method to apply thermal cycling on cylindrical sealant samples with a central borehole. The

temperatures of the sample and injected water, and the rate and the duration of the injection are the same as in Li and Pluymakers (2024). Microstructural scanning, pycnometry and mechanical tests are carried out before and after experiments to examine the effects of thermal cycling on sealants under confinement. Additionally, together with reviewing the results in Li and Pluymakers (2024), we aim to identify the key properties of a sealant that determine its performance through strong thermal cycling, thereby contributing to the advancement of wellbore sealant design and testing for CCS applications.

## 2 Experimental Materials, Apparatus, and Methodologies

In our study, we employ cylindrical sealant samples (diameter 3 cm, length 7 cm) with a diameter 4 mm central borehole along the vertical axis. The samples represent four different compositions, as outlined in Table 1: S1 corresponds to a conventional OPC-based blend, S2 to an ultra-reduced permeability OPC-based blend for field design, S3 to an OPC-based blend incorporating $CO_2$-sequestering additives also with modified mechanical properties, and S4 to a CAC-based blend designed to be highly acid resistant for $CO_2$ storage environment. These sealants include compositions representative of currently-utilized wellbore sealing materials in aged oil and gas wells targeted for CCS (S1 and S2, serving as references), and specially engineered blends intended for application in newly drilled CCS wells (S3 and S4). Table 1 provides an overview of the four different sealant compositions and their respective Technology Readiness Levels (TRLs).

| Sealant | Composition | TRL |
|---|---|---|
| S1 | 1.90 SG class G cement with 35% BWOC silica flour | 7: Proven technology |
| S2 | 1.90 SG ultra-reduced permeability class G cement with 35% BWOC silica flour, with high silica fume concentration and expansion agent in form of dead-burnt MgO | 7: Proven technology |
| S3 | 1.90 SG class G cement with 35% BWOC silica flour, with silica fume, expansion agent in form of dead-burnt MgO, and $CO_2$-sequestering additives based on olivine minerals | 3: Prototype tested |
| S4 | 1.80 SG calcium aluminate-based blend | 7: Proven technology |

**Table 1**: an overview of four sealant compositions and their TRLs.

All samples used in this study are cast and cured by Halliburton AS Norway, following the guidelines stipulated in API Recommended Practice 10B-2 (API RP 10B-2, 2013). This process involves a water/cement ratio of 0.4, coupled with curing conditions at 150°C and 30 MPa for a duration of 28 days. The elevated temperature and pressure settings are instrumental in driving chemical reactions toward near completion during the curing process, thereby ensuring minimal variation in the mechanical and thermal properties of our samples throughout the study period. Post-curing, all samples are submerged in fresh water and stored at room temperature until use. Before each experiment in our study, all samples undergo thorough drying in an air-circulated oven (model UF75, Memmert). The samples are placed in the oven at room temperature, subjected to a ramping rate of 2.5°C/min until reaching 80°C, and held at 80°C for 2 days to achieve complete dewatering. Following this, the samples are gradually cooled down to room temperature at the same ramping rate. These procedures are implemented to minimize the adverse impact of associated thermal stresses during both the heating and cooling phases, ensuring the preservation of sample integrity without any compromise.

Before commencing any thermal-cycling experiments, we perform Brazilian disc tests on dried disc sealant samples (diameter 3 cm, thickness 1.5 cm) to measure the tensile strength, $\sigma_T$, of the sealants. The Brazilian disc testing is carried out using a 50 kN loading frame, with displacement controlled by two high-precision linear variable differential transformers (LVDTs) with a 2 mm range. The tests are performed in displacement control mode with a ramping rate of 0.0005 mm/s. The equation to calculate tensile strength is given by Claesson and Bohloli, (2002) :

$$\sigma_t = \frac{2\,P}{\pi\,D\,L} \tag{1}$$

where $P$ is the load at which the sample fails, $D$ the diameter, and $L$ the thickness of the disc sample.

In addition, we use a thermomechanical analyzer (PerkinElmer, TMA 4000) to measure the linear thermal expansion coefficient and a helium gas pycnometer (Anton Paar, Ultrapyc 5000) to measure the effective porosity of the dried sealants. Table 2 provides the tensile strength, thermal expansion coefficient, and effective porosity of the dried sealants of all four compositions. Other mechanical properties including unconfined compression strength (UCS), Young's modulus, and Poisson's ratio, bulk density, and thermal properties including thermal conductivity, specific heat capacity, and thermal diffusivity were measured by Li and Pluymakers (2024) and are also provided here in Table 2.

Note that the tensile strength, thermal expansion coefficient, and effective porosity of each sealant composition listed in Table 2 are averaged based on measurements of three samples each made at an interval of one month. This is implemented to ensure that the obtained results aren't influenced by an ongoing cement curing process, i.e. to verify that the curing procedure performed by Halliburton in sample preparation was sufficient to achieve a stable mechanical and thermal state of the sealants. The relatively small standard deviation implies that our measurements are repeatable, and those properties of sealants have not changed throughout our study duration.

| Sealant | Unconfined compressive strength [MPa] | Young's modulus [GPa] | Poisson's ratio [-] | Tensile Strength [MPa] | Bulk density [kg/m$^3$] | Thermal conductivity [W/(m·K)] | Specific heat capacity [J/(kg·K)] | Thermal diffusivity [mm$^2$/s] | Linear thermal expansion coefficient [$10^{-6}$ °C$^{-1}$] | Effective porosity by helium pycnometry [%] |
|---|---|---|---|---|---|---|---|---|---|---|
| S1 | 99.8 | 13.4 | 0.143 | 3.63±0.35 | 1455 | 0.82±0.04 | 878±18 | 0.64 | 6.89±0.20 | 35.6±1.9 |
| S2 | 81.1 | 12.0 | 0.162 | 5.51±0.32 | 1507 | 0.93±0.03 | 936±11 | 0.66 | 10.93±0.62 | 26.8±2.1 |
| S3 | 33.4 | 6.1 | 0.139 | 6.79±0.15 | 1374 | 1.04±0.02 | 684±13 | 1.11 | 9.40±0.12 | 42.2±0.9 |
| S4 | 34.3 | 6.6 | 0.172 | 3.92±0.10 | 1497 | 0.89±0.02 | 970±21 | 0.61 | 12.32±0.53 | 37.5±1.6 |

**Table 2**: properties of the four sealants, as measured before thermal treatment. Tensile strength, linear thermal expansion coefficient, and effective porosity are measured in this study. UCS, Young's modulus, Poisson's ratio, bulk density, thermal conductivity, specific heat capacity, and thermal diffusivity were measured by Li and Pluymakers (2024).

To visualize the effects of thermal cycling on sealant samples, we use an X-ray micro-computed tomography (micro-CT) scanner (model Nanotom 180 NF, Phoenix X-ray Systems & Services GmbH) to scan samples before and after thermal treatment at a voxel resolution of 32 $\mu$m. We then use Phoenix datos software (version 2.0, GE Measurement & Control solutions) to post-process the images and further use Avizo software (version 2020.2, ThermoFisher Scientific) to construct the 3D microstructure in samples at a voxel resolution of 32 $\mu$m before and after experiments. Due to the limitation of our technique, micro-cracks and voids of size below 32 $\mu$m cannot be detected. Using Avizo, we quantify the volume of micro-cracks and voids, and the porosity of the sample attributed to these features. The workflow of image analysis is detailed in the Appendix of Li and Pluymakers (2024). In addition, we

measure effective porosity, and UCS after the experiments to study how thermal cycling affects the macroscopic property and the strength of sealant samples. UCS tests are conducted using the same procedures described in Li and Pluymakers (2024). Table 3 shows all samples to be tested and the experimental scheme.

| No. | Sample name | Sealant composition | Confining pressure [MPa] | Experiment scheme |
|---|---|---|---|---|
| 1 | S1H-1 | S1, OPC blend | 1.5 | helium pycnometry ↓ micro-CT ↓ thermal cycling ↓ micro-CT ↓ helium pycnometry ↓ UCS |
| 2 | S1H-1 | | 10 | |
| 3 | S2H-1 | S2, OPC blend with ultra-reduced permeability | 1.5 | |
| 4 | S2H-2 | | 10 | |
| 5 | S3H-1 | S3, OPC blend with $CO_2$-sequestering additives | 1.5 | |
| 6 | S3H-2 | | 10 | |
| 7 | S4H-1 | S4, CAC blend | 1.5 | |
| 8 | S4H-2 | | 10 | |

**Table 3**: an overview of all samples to be tested and the experimental scheme.

In our study, we use a triaxial deformation apparatus (Figure 1) capable of loading a sealant sample in a pressure vessel at a confining pressure of up to 70 MPa, with a maximum axial force up to 300 kN (equivalent to 424 MPa axial stress on a cylinder sample with a diameter of 3 cm). As shown in Fig.1, a furnace is used to achieve an elevated temperature up to 150 ºC in the vessel. The sample, jacketed by a heat-shrinkable FEP (fluorinated ethylene propylene) tube (thickness 0.5 mm), is mounted between the upper and lower axial pistons. In both pistons, pore fluid lines are fitted to allow water injection through the sample. During the experiments, the triaxial vessel is filled with heat transfer oil (Shell Thermia oil B) that provides the confining pressure and transmits the heat. Two LVDTs (2 mm range) mounted parallel to the sample, and one circumferential strain gauge (10 mm range) mounted around the sample are used to monitor axial and radial deformation, respectively. Two thermocouples (type K, NI-9219, National Instruments, max. reading 700 °C, accuracy ±1 °C) are installed to measure the temperature $T_s$ in the middle on the outer surface, and $T_t$ on the top of the sample. During thermal cycling experiments, cool-water bath is running through the annulus in the vessel shell to protect the electronics of the apparatus from elevated temperature.

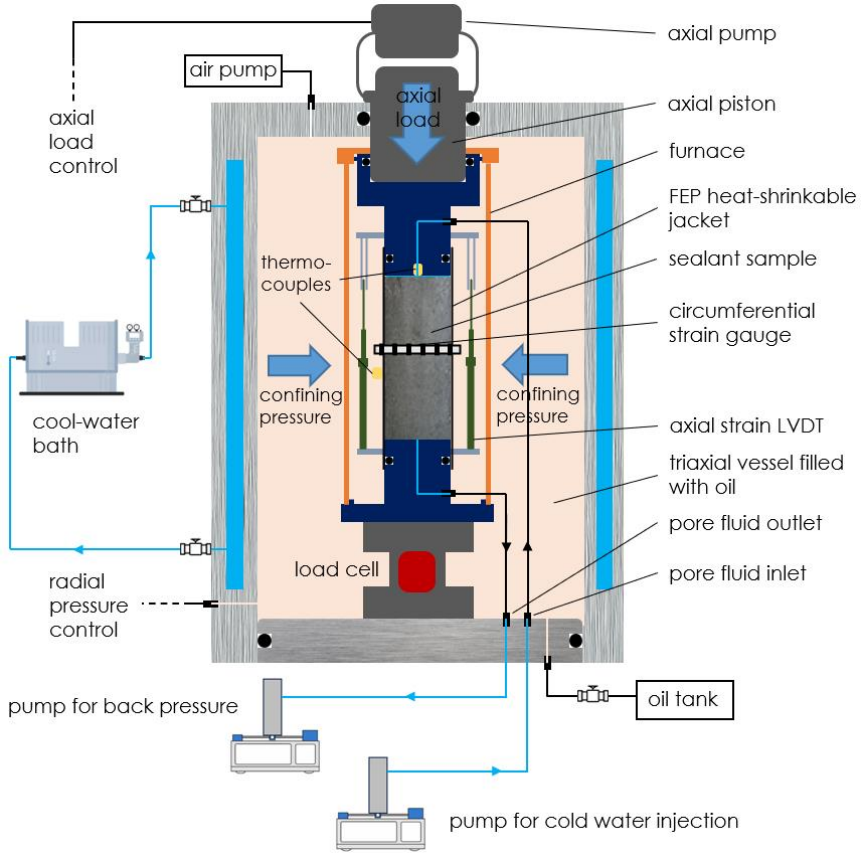


**Fig. 1.** Schematic of the triaxial deformation apparatus with sealant sample mounted inside the pressure vessel. The drawing does not adhere to the actual scale.

In thermal cycling experiments, to mimic an in-situ state of stress, we load the sample either at a confining pressure of 1.5 MPa with an axial stress of 4 MPa, or at a confining pressure of 10 MPa with an axial stress of 15 MPa. We then heat the pressure vessel filled with oil to 120 ºC at a ramping rate of 2.2 °C/min, and maintain the system at this temperature for half an hour to allow the sample to be fully heated. We then inject 20 ºC water from top to bottom through the sample using a high-pressure syringe pump (model 1000D, Teledyne ISCO, range: 0.001 to 408 mL/min, accuracy: 0.5% of setpoint) at 80 mL/min for 2 min, with a back pressure controlled by another syringe pump (model 260D, Teledyne ISCO, range: 0.001 to 107 mL/min, accuracy: 0.5% of setpoint). The back pressure is set at 0.5 MPa in experiments under 1.5 MPa confinement, and 6 MPa in experiments under 10 MPa confinement. After 2 min of injection, we stop for 12 min to let the system reheat the sample back to 120ºC. We repeat this for eight cycles. For each sealant composition, we test two samples, with one at 1.5 MPa confinement and one at 10 MPa confinement (Table 3).

Figure 2 illustrates the temperature variations at different positions of sample S1H-1 during the experiment. These changes serve as a representation of experiments conducted on all samples. As depicted, temperatures on the outer surface, $T_s$, and on the top (flow inlet), $T_t$, of the sample reach 120 ºC following gradual heating by the furnace. These temperatures remain constant at 120 ºC until the commencement of thermal cycling. Upon initial water injection, $T_t$ rapidly decreases to 50 ºC within 2 minutes (at a rate of 35 ºC/min), while $T_s$ decreases to 112 ºC within the same timeframe. Subsequently, both temperatures equilibrate back to the system temperature at 120 ºC, ready for the next injection

cycle. This temperature fluctuation recurs eight times before the temperatures gradually decrease to room temperature upon shutting down the furnace.

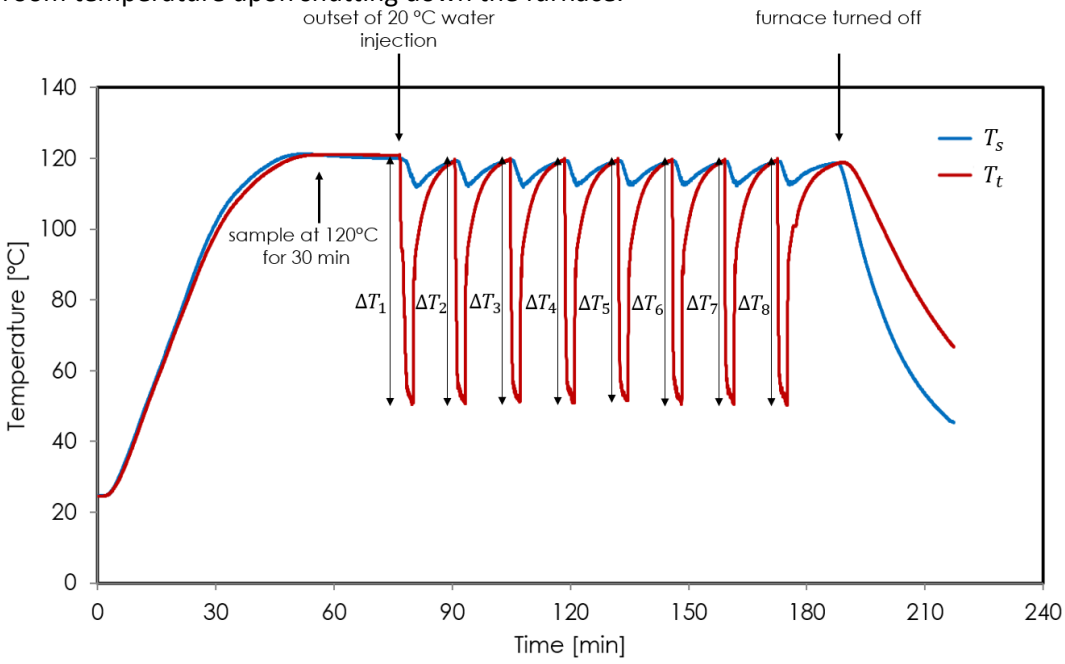


**Fig. 2.** Temperature variations at the outer surface ($T_s$) and inlet ($T_t$) of sample S1H-1 during thermal-cycling experiment. These variations serve as a representation of experiments conducted on all samples.

As shown in Fig.2, the most significant temperature fluctuation is observed near the sample inlet region, where the thermal cycling induces the highest thermal stress throughout the sample. We determine this maximum thermal stress, $\sigma_T$, using the below equation (Carter and Paul, 1991; Callister et al., 2007):

$$\sigma_T = E \cdot \gamma \cdot \Delta T_t \quad (2)$$

where $E$ is Young's modulus, $\gamma$ the thermal expansion coefficient of the sealant, and $\Delta T = \frac{\sum_1^8 \Delta T_{t_i}}{8}$ is the average temperature drop at the inlet of the sample within one injection cycle.

## 3 Results

### 3.1 Microstructure and porosities of sealant samples before and after thermal cycling under confinement

Figures 3 to 6 show the microstructure of the two samples, one under 1.5 MPa confinement and another under 10 MPa confinement, before and after thermal cycling experiments for each of the four sealant compositions S1 to S4, respectively. These images show the structure of voids of size larger than 32 $\mu$m in samples. There are pre-existing voids in samples of S1 and S3 compositions before thermal treatment (Figs. 3 and 5). Samples of S2 and S4 do not have pre-existing voids, so orthogonal slices are provided in Figs. 4 and 6 to illustrate the intactness of the samples before thermal treatment.

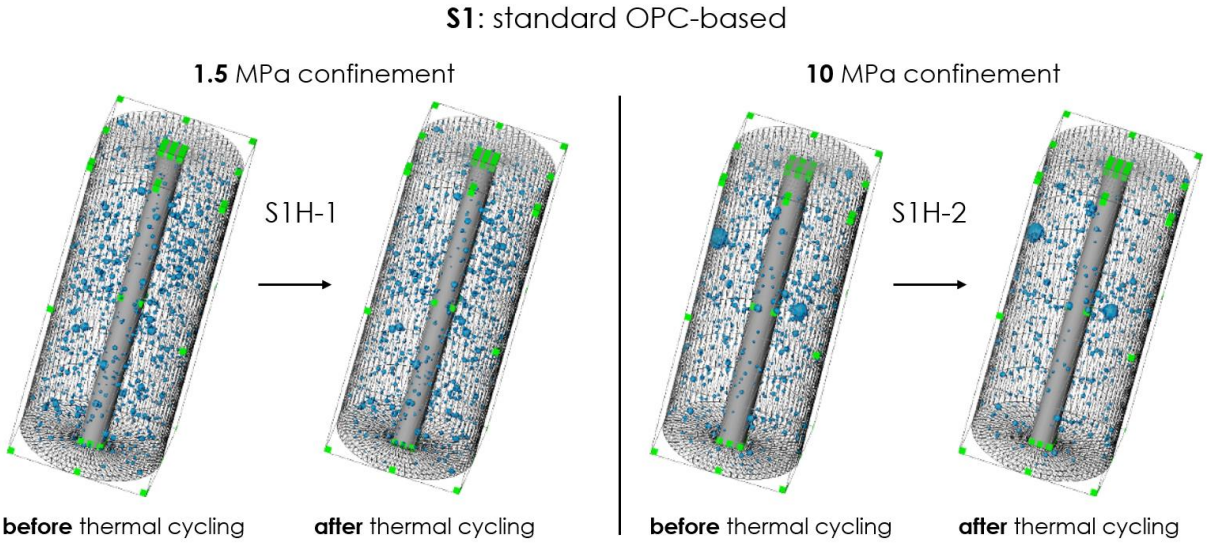


**Fig. 3.** Microstructure of samples S1H-1(left, under 1.5 MPa confinement) and S1H-2 (right, under 10 MPa confinement) before and after thermal cycling. Voxel resolution of 32 $\mu$m. Samples are of sealant composition S1, standard OPC-based. No cracks or evident alterations are observed in either sample following thermal treatment.

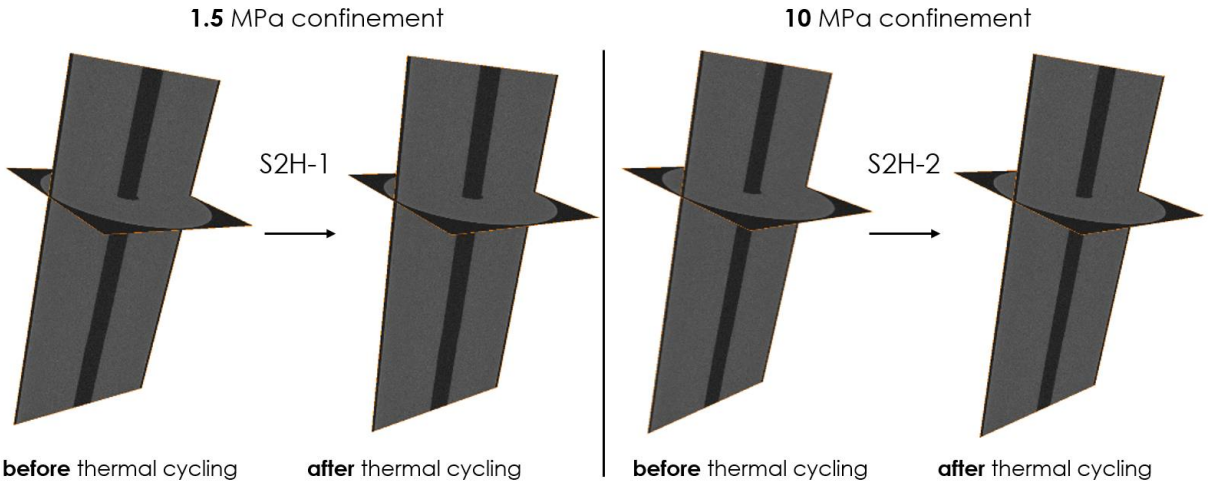


**Fig. 4.** Microstructure of samples S2H-1(left, under 1.5 MPa confinement) and S2H-2 (right, under 10 MPa confinement) before and after thermal cycling. Voxel resolution of 32 $\mu$m. Samples are of sealant composition S2, ultra-reduced permeability OPC-based. No cracks or evident alterations are observed in either sample following thermal treatment.

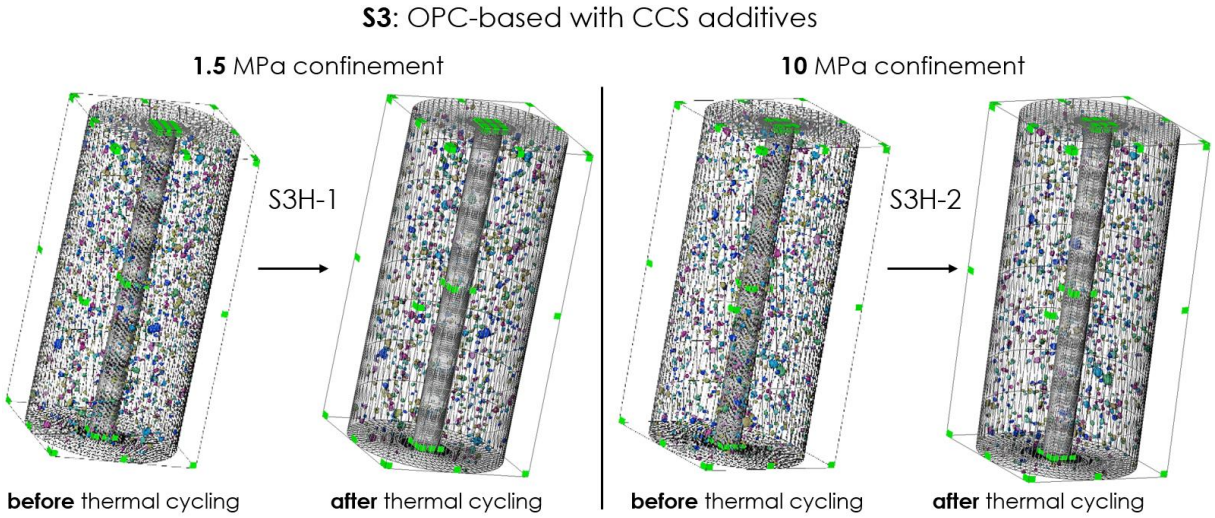


**Fig. 5.** Microstructure of samples S3H-1(left, under 1.5 MPa confinement) and S3H-2 (right, under 10 MPa confinement) before and after thermal cycling. Voxel resolution of 32 $\mu$m. Samples are of sealant composition S3, OPC-based with CCS additives. No cracks or evident alterations are observed in either sample following thermal treatment.

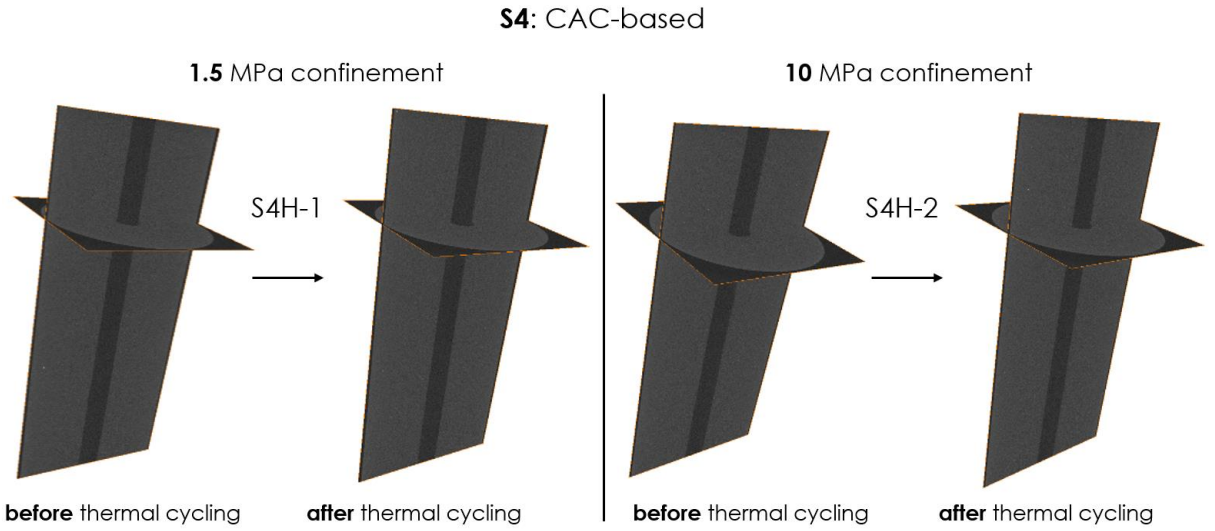


**Fig. 6.** Microstructure of samples S4H-1(left, under 1.5 MPa confinement) and S4H-2 (right, under 10 MPa confinement) before and after thermal cycling. Voxel resolution of 32 $\mu$m. Samples are of sealant composition S4, CAC-based. No cracks or evident alterations are observed in either sample following thermal treatment.

For all samples of sealants S1 to S4, thermal cycling under confinement of either 1.5 MPa or 10 MPa hasn't induced any visible cracks of size larger than 32 µm. Table 4 shows the overall void volume in the sample before and after thermal treatment ($V_0$ and $V_{TC}$, respectively), the percentage decrease in void volume, porosity by micro-CT of the intact sample ($\phi_{CT}^0$), and the porosity decrease by micro-CT ($\Delta\phi_{CT}$).

| Sample name | Sealant composition | Confinement [MPa] | Total volume of voids [mm$^3$] | | | $\phi_{CT}^0$ , [%] | $\Delta\phi_{CT} = \frac{V_0 - V_{TC}}{V_{sample}}$ , [%] |
|---|---|---|---|---|---|---|---|
| | | | $V_0$ | $V_{TC}$ | $\frac{V_0 - V_{TC}}{V_0}$ , [%] | | |
| S1H-1 | S1, OPC blend | 1.5 | 201 | 192 | 4 | 0.406 | 0.02 |
| S1H-2 | | 10 | 232 | 207 | 11 | 0.469 | 0.05 |
| S3H-1 | S3, OPC blend with $CO_2$-sequestering additives | 1.5 | 158 | 146 | 8 | 0.319 | 0.02 |
| S3H-2 | | 10 | 141 | 114 | 19 | 0.285 | 0.05 |

**Table 4**: the overall void volume in the sample before and after thermal treatment ($V_0$ and $V_{TC}$, respectively), the percentage decrease in void volume, porosity by micro-CT of the intact sample ($\phi_{CT}^0$), and the porosity decrease by micro-CT ($\Delta\phi_{CT}$). Note that the voids, identifiable through micro-CT are larger than 32 $\mu$m. The data presented in this table pertains only to S1 and S3 samples, as S2 and S4 samples are densely packed and exhibit no discernible voids before and after thermal treatment.

For sealants S1 and S3, there is a reduction in void volume, indicating increased compactness following thermal cycling under either 1.5 MPa or 10 MPa confinement. The compacting effect is more noticeable under higher confinement at 10 MPa, leading to a greater decrease in porosity as observed by micro-CT. Note that the porosity determined by our micro-CT (32 $\mu$m/voxel) is significantly lower than the effective porosity measured by the helium pycnometer (refer to Table 2). This difference likely arises from the fact that pores responsible for the majority of the effective porosity of hardened cementitious materials, such as our sealants, exist below the microscopic scale (Frías and Cabrera, 2000; Pipilikaki and Beazi-Katsioti, 2009) and therefore cannot be detected by our micro-CT.

Figure 7 illustrates the effective porosity of samples from all four sealants before and after thermal treatment under 1.5 MPa (left) and 10 MPa confinement (right), as measured using helium pycnometer. Compared to the porosities determined by micro-CT, the porosities measured by pycnometer for all sealant samples are at much higher amplitude and exhibit more notable decrease following thermal-cycling experiments under either 1.5 MPa or 10 MPa confinement. Particularly, under a higher confinement of 10 MPa, the reduction in porosities is more pronounced for all four sealants. The combination of visible micro-CT porosities and effective porosities by pycnometer corroborates that the thermal cycling hasn't compromised the integrity of the sealant in our experiments conducted under confinement. Instead, it suggests that the confinement serves to compact the sealant, with greater compacting effects observed at higher confinement.

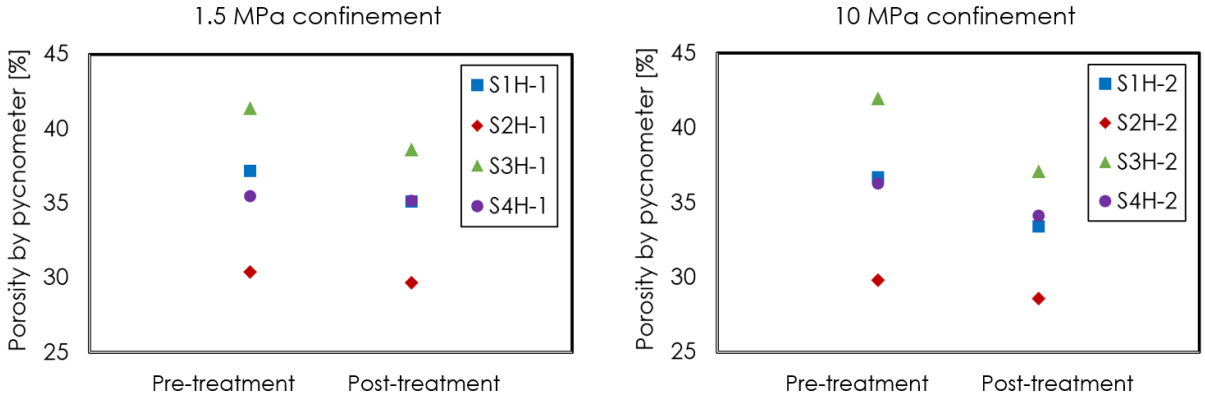


**Fig. 7.** Effective porosity of samples from all four sealants before and after thermal treatment under 1.5 MPa (left) and 10 MPa confinement (right), as measured using helium pycnometer.

### 3.2 UCS of sealant samples before and after thermal cycling under confinement

Figure 8 shows the unconfined compressive strength (UCS) of both intact samples and those subjected to thermal-cycling experiments under 1.5 MPa and 10 MPa confinement for four different sealants. Following thermal cycling under confinement, the UCS of samples from all four sealants demonstrates an increase, with a more pronounced enhancement under higher confinement. The marginal decrease in UCS observed for sample S4H-1 does not significantly affect the overall trend.

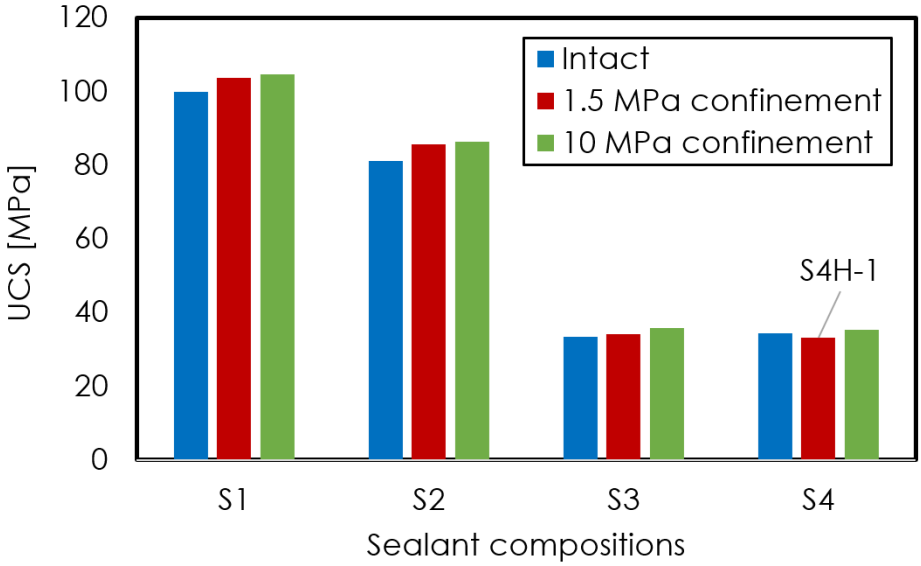


**Fig. 8.** UCS of both intact samples and those subjected to thermal-cycling experiments under 1.5 MPa and 10 MPa confinement for four different sealants.

In contrast to unconfined experiments in Li and Pluymakers (2024), where thermal cycling compromised the integrity of all sealants except S3 by causing a decrease in UCS with the formation of cracks, the confinement in this study not only effectively mitigates the detrimental effects of thermal cycling on sealant integrity without causing any sample breakage but also strengthens the sealants with reducing porosities (discussed in subsection 3.1).

## 4 Discussion

In this study, we expand upon the unconfined experiments conducted by Li and Pluymakers (2024) by examining the effects of thermal cycling, with the same intensity, duration, and frequency as outlined in

the flow-through experiments of Li and Pluymakers (2024), on four sealants under different confinements for CCS applications. These sealants include two reference OPC-based sealants (S1 and S2), and two newly-designed blends intended for future CCS wells (S3 and S4). S3 is based on OPC but with $CO_2$-sequestering additives, and S4 is based on calcium aluminate cement (CAC).

In the presence of confinements, all sealant samples can well maintain their sealing integrity throughout thermal cycling, contrasting with the loss of integrity and emergence of thermally-induced cracks observed in unconfined experiments. The cracks observed in the unconfined experiments predominantly originate from tensile stresses incurred during the rapid cooling phases of the samples. During abrupt cooling, the heat concentrated near the borehole dissipates rapidly into the cold water within the borehole, resulting in a sharp temperature decline and subsequent shrinkage in that vicinity, thereby initiating thermal stresses. Regions further from the borehole undergo a delayed reaction, experiencing a lesser temperature drop and corresponding shrinkage. As thermal stresses induced by this thermomechanical deformation propagate temporally and spatially throughout the sample, they oppose the tensile strength of the sealants. Figure 9 illustrates the tensile strength of the four sealants, along with the thermal stresses induced by confined and unconfined thermal-cycling experiments on the four sealants. Note that thermal stresses referenced herein represent the maximum values generated in the vicinity of the borehole inlet of the sample, coinciding with the location of the most significant temperature drop. Additionally, thermal diffusivity determined by Li and Pluymakers (2024) is depicted in Fig. 9, reflecting the transient heat transfer rate within the sealants. Sealants with higher diffusivity exhibit more efficient heat conduction, resulting in a lower loading rate of the thermal stress.

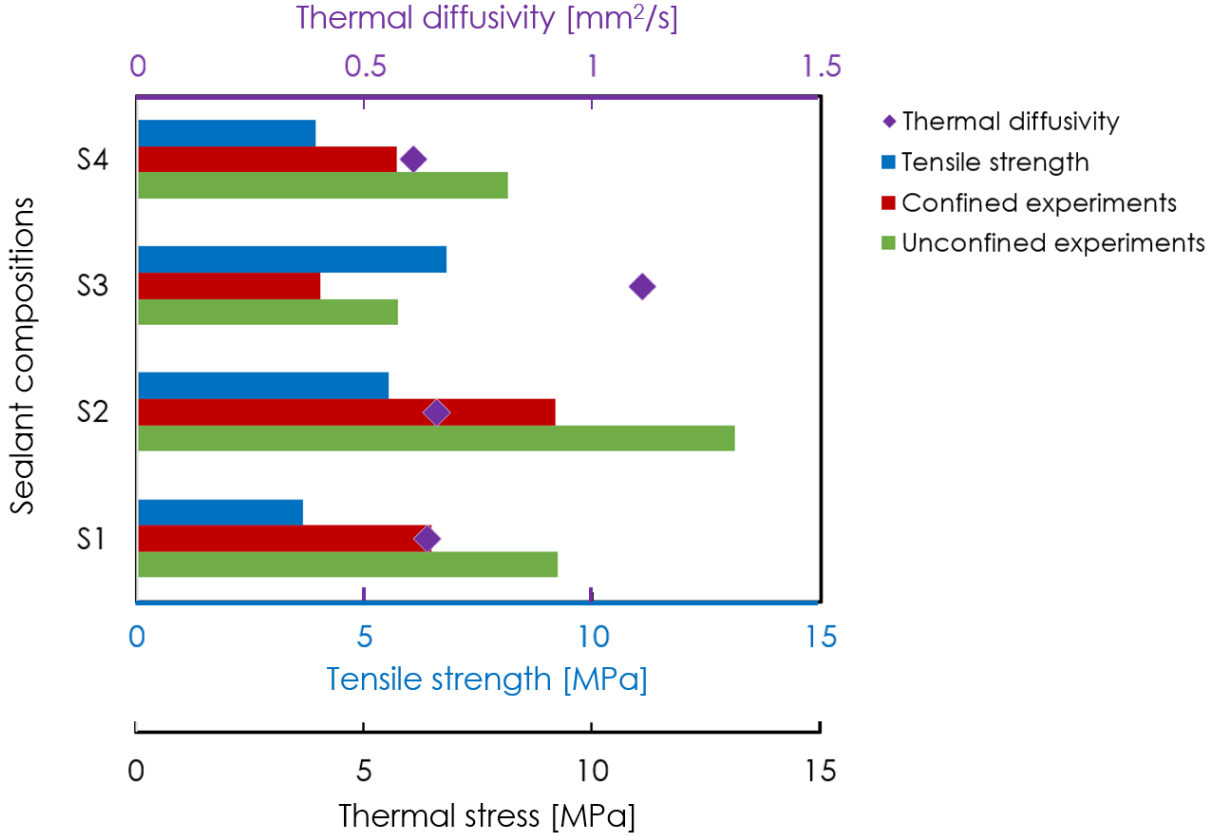


**Fig. 9.** Thermal diffusivity and tensile strength of the four sealants, along with the thermal stresses induced by confined and unconfined thermal-cycling experiments on the four sealants. Thermal diffusivity and temperature changes used for thermal stress calculations in unconfined experiments are from Li and Pluymakers (2024).

The discrepancy in thermal stresses between unconfined and confined experiments arises primarily from the diminished temperature drop experienced under confinement during thermal cycling. In the triaxial deformation setup (Fig. 1), the longer path that the injected water must traverse to reach the sample results in its heating, thereby reducing its capacity to induce a temperature drop of equivalent magnitude to that observed in unconfined experiments. Despite this constraint, thermal stresses induced by confined thermal cycling remain greater than the tensile strength for all sealants except S3, whereas those from unconfined thermal cycling are even more pronounced.

In experiments without confinement, thermal stresses surpass the tensile strength, leading to the formation of tensile cracks in samples of all sealants except S3. The exceptional performance of sealant S3 can be attributed to its comparatively high tensile strength and thermal diffusivity, which enable it to withstand thermal cycling without compromising integrity. In our study, although thermal stresses still exceed the tensile strength of all sealants excluding S3, the presence of confinement offers structural support to the sealant samples, augmenting their stiffness and reducing the likelihood of cracks resulting from thermal cycling. Furthermore, confinement strengthens the sealants, leading to an increase in UCS.

In light of the preceding discussion, concerning the future design of sealants to withstand thermal cycling and sustain sealing integrity for CCS applications, an ideal sealant candidate should possess high tensile strength, high thermal diffusivity, and minimal susceptibility to thermal stress accumulation, indicated by low Young's modulus and low thermal expansion coefficient.

## 5 Conclusions

Building upon prior research conducted by Li and Pluymakers (2014) focusing on the effects of thermal cycling on four different sealant compositions in unconfined conditions, this study extends the investigation by using a triaxial deformation setup to assess their behavior under thermal cycling with confinement. The sealants examined include two conventional OPC-based sealants (S1 and S2) and two novel blends tailored for prospective application in CCS wells (S3 and S4). S3 integrates OPC with $CO_2$-sequestering additives, while S4 is formulated based on calcium aluminate cement (CAC).

Our findings reveal that, notwithstanding thermal stresses exceeding tensile strength for all sealants except S3, confinement effectively mitigates the adverse effects of thermal cycling on sealant integrity without causing any sample breakage, by providing structural support to the sealant and enhancing its stiffness. In addition, confinement reduces porosity and augments the UCS of the samples, which indicates the reinforcing effect of confinement on sealant performance, particularly evident at higher confinement levels.

In contrast, experiments conducted without confinement (as observed in Li and Pluymakers, 2024) demonstrate that thermal stresses surpass the tensile strength, leading to the development of tensile cracks in samples of all sealants except S3. The superior performance of S3 is attributed to its comparably high tensile strength and thermal diffusivity.

Overall, this study underscores the significance of considering confinement effects when evaluating sealant performance under thermal cycling. The findings suggest that sealants with high tensile strength, high diffusivity, low Young's modulus, and low expansion coefficient are optimal candidates for enduring thermal cycling in CCS well environments. Together with Li and Pluymakers (2014), our study elucidates the interplay between sealant properties and confinement conditions, thereby offering valuable insights into the design and testing of sealants for CCS applications.

**Acknowledgement:**
The CEMENTEGRITY project is funded through the ACT program (Accelerating CCS Technologies, Horizon2020 Project No 691712).
Financial contributions from the Research Council of Norway (RCN), the Netherlands Enterprise Agency (RVO), the Department for Energy Security & Net Zero (DESNZ, UK), and Harbour Energy are gratefully acknowledged. We thank Jan Etienne, Ellen Meijvogel-de Koning, and Jens van den Berg in Geoscience & Engineering Laboratory at Delft University of Technology, the Netherlands, for their technical support.

**References**

Albawi, A., De Andrade, J., Torsæter, M., Opedal, N., Stroisz, A., & Vrålstad, T. (2014, February). Experimental set-up for testing cement sheath integrity in arctic wells. In *OTC Arctic Technology Conference*. OnePetro. https://doi.org/10.4043/24587-MS.

Alnes, H., Eiken, O., Nooner, S., Sasagawa, G., Stenvold, T., & Zumberge, M. (2011). Results from Sleipner gravity monitoring: Updated density and temperature distribution of the $CO_2$ plume. *Energy Procedia*, **4**, 5504-5511. https://doi.org/10.1016/j.egypro.2011.02.536.

Barborak, R. (2010). Calcium aluminate cement concrete (class cac concrete) txdot special specification ss-4491 tip sheet. Construction and Bridge Divisions, Texas Department of Transportation: Austin, TX, USA.

Budinis, S., Krevor, S., Mac Dowell, N., Brandon, N., & Hawkes, A. (2018). An assessment of CCS costs, barriers and potential. *Energy strategy reviews*, **22**, 61-81. https://doi.org/10.1016/j.esr.2018.08.003.

Bui, M., Adjiman, C. S., Bardow, A., Anthony, E. J., Boston, A., Brown, S., ... & Mac Dowell, N. (2018). Carbon capture and storage (CCS): the way forward. *Energy & Environmental Science*, **11**(5), 1062-1176. DOI: 10.1039/C7EE02342A.

Callister, W. D., Rethwisch, D. G., Blicblau, A., Bruggeman, K., Cortie, M., Long, J., ... & Mitchell, R. (2007). Materials science and engineering: an introduction (Vol. **7**, pp. 665-715). *New York: John wiley & sons*.

Carey, J. W., Wigand, M., Chipera, S. J., WoldeGabriel, G., Pawar, R., Lichtner, P. C., Wehner, S. C., Raines, M. A., & Guthrie Jr, G. D. (2007). Analysis and performance of oil well cement with 30 years of $CO_2$ exposure from the SACROC Unit, West Texas, USA. *International journal of greenhouse gas control*, **1**(1), 75-85. https://doi.org/10.1016/S1750-5836(06)00004-1.

Carpenter, R. B., Brady, J. L., & Blount, C. G. (1992). The effects of temperature and cement admixes on bond strength. *Journal of Petroleum Technology*, **44**(08), 936-941. https://doi.org/10.2118/22063-PA.

Carter, G. F., & Paul, D. E. (1991). Materials science and engineering. *ASM international*.

Claesson, J., & Bohloli, B. (2002). Brazilian test: stress field and tensile strength of anisotropic rocks using an analytical solution. *International Journal of Rock Mechanics and Mining Sciences*, **39**(8), 991-1004. https://doi.org/10.1016/S1365-1609(02)00099-0.

De Andrade, J., Sangesland, S., Todorovic, J., & Vrålstad, T. (2015, April). Cement sheath integrity during thermal cycling: a novel approach for experimental tests of cement systems. In *SPE Bergen one day seminar*. OnePetro. https://doi.org/10.2118/173871-MS.

Dugonjic-Bilic, F., Tiemeyer, C., & Plank, J. (2011, April). Study on admixtures for calcium aluminate phosphate cement useful to seal CCS wells. In *SPE International Symposium on Oilfield Chemistry*. OnePetro. https://doi.org/10.2118/141179-MS.

Eiken, O., Ringrose, P., Hermanrud, C., Nazarian, B., Torp, T. A., & Høier, L. (2011). Lessons learned from 14 years of CCS operations: Sleipner, In Salah and Snøhvit. *Energy procedia*, **4**, 5541-5548. https://doi.org/10.1016/j.egypro.2011.02.541.

Frías, M., & Cabrera, J. (2000). Pore size distribution and degree of hydration of metakaolin–cement pastes. *Cement and Concrete Research*, **30**(4), 561-569. https://doi.org/10.1016/S0008-8846(00)00203-9.

Haszeldine, R. S. (2009). Carbon capture and storage: how green can black be? *Science*, **325**(5948), 1647-1652. DOI: 10.1126/science.1172246.

Kirby, G. A. (2001). Depth Mapping and Characterisation of the Utsira Sand Saline Aquifer, Central and Northern North Sea: *British Geological Survey Report* CR/01/218N. British Geological Survey.

Kvassnes, A., & Clausen, J. A. (2020). U.S. Patent No. 10,774,001. Washington, DC: U.S. Patent and Trademark Office.

Kvassnes, A., & Clausen, J. A. (2021). U.S. Patent No. 11,014,851. Washington, DC: U.S. Patent and Trademark Office.

Lescanne, M., Hy-Billiot, J., Aimard, N., & Prinet, C. (2011). The site monitoring of the Lacq industrial CCS reference project. *Energy Procedia*, **4**, 3518-3525. https://doi.org/10.1016/j.egypro.2011.02.279.

Lesti, M., Tiemeyer, C., & Plank, J. (2013). $CO_2$ stability of Portland cement based well cementing systems for use on carbon capture & storage (CCS) wells. *Cement and concrete research*, **45**, 45-54. https://doi.org/10.1016/j.cemconres.2012.12.001.

Li, K., & Pluymakers, A. M. (2024). Effects of thermal shocks on integrity of existing and newly-designed sealants for CCS applications. *International Journal of Greenhouse Gas Control*, **133**, 104103. https://doi.org/10.1016/j.ijggc.2024.104103.

Lund, H., Torsæter, M., & Munkejord, S. T. (2015, April). Study of thermal variations in wells during $CO_2$ injection. In *SPE Bergen One Day Seminar*. OnePetro. https://doi.org/10.2118/173864-MS.

Metz, B., Davidson, O., De Coninck, H. C., Loos, M., & Meyer, L. (2005). IPCC special report on carbon dioxide capture and storage. Cambridge: Cambridge University Press.

Parker, M. E., Meyer, J. P., & Meadows, S. R. (2009). Carbon dioxide enhanced oil recovery injection operations technologies. *Energy Procedia*, **1**(1), 3141-3148. https://doi.org/10.1016/j.egypro.2009.02.096.

Pipilikaki, P., & Beazi-Katsioti, M. (2009). The assessment of porosity and pore size distribution of limestone Portland cement pastes. *Construction and Building Materials*, **23**(5), 1966-1970. https://doi.org/10.1016/j.conbuildmat.2008.08.028.

Roy, P., Walsh, S. D., Morris, J. P., Iyer, J., Hao, Y., Carroll, S., ... & Torsæter, M. (2016, June). Studying the impact of thermal cycling on wellbore integrity during $CO_2$ injection. In *50th US Rock Mechanics/Geomechanics Symposium*. OnePetro.

Samara, H., Al-Eryani, M., & Jaeger, P. (2022). The role of supercritical carbon dioxide in modifying the phase and interfacial properties of multiphase systems relevant to combined EOR-CCS. *Fuel*, **323**, 124271. https://doi.org/10.1016/j.fuel.2022.124271.

Santra, A., & Sweatman, R. (2011). Understanding the long-term chemical and mechanical integrity of cement in a CCS environment. *Energy Procedia*, **4**, 5243-5250. https://doi.org/10.1016/j.egypro.2011.02.503.

Selma, L., Seigo, O., Dohle, S., & Siegrist, M. (2014). Public perception of carbon capture and storage (CCS): A review. *Renewable and Sustainable Energy Reviews*, **38**, 848-863. https://doi.org/10.1016/j.rser.2014.07.017.

Vilarrasa, V., & Rutqvist, J. (2017). Thermal effects on geologic carbon storage. *Earth-science reviews*, **165**, 245-256. https://doi.org/10.1016/j.earscirev.2016.12.011.

Yoo, B. Y., Choi, D. K., Kim, H. J., Moon, Y. S., Na, H. S., & Lee, S. G. (2013). Development of $CO_2$ terminal and $CO_2$ carrier for future commercialized CCS market. *International Journal of Greenhouse Gas Control*, **12**, 323-332. https://doi.org/10.1016/j.ijggc.2012.11.008.

Zhang, K., Lau, H. C., & Chen, Z. (2022). Extension of $CO_2$ storage life in the Sleipner CCS project by reservoir pressure management. *Journal of Natural Gas Science and Engineering*, **108**, 104814. https://doi.org/10.1016/j.jngse.2022.104814.